Journal of Applied Fluid Mechanics, Vol. 12, No. 6, pp. 2017-2030, 2019.
Available online at www.jafmonline.net, ISSN 1735-3572, EISSN 1735-3645.
DOI: 10.29252/jafm.12.06.29880

Angle of Attack Investigations on the Performance of a Diverterless Supersonic Inlet

R. Askari [1], M. R. Soltani [1], K. Mostoufi [1], A. Khajeh Fard [2] and M. Abedi [1]

[1] *Department of Aerospace Engineering, Sharif University, Tehran, Iran*
[2] *Department of Aerospace Engineering, Shahid Sattari University, Tehran, Iran*

†*Corresponding Author Email:reza2@uw.edu*

(Received November 29, 2018; accepted March 5, 2019)

ABSTRACT

An extensive experimental investigation to study the effects of angle of attack (*AOA*) on the performance of a body-integrated supersonic inlet has been carried out. The present inlet, known as Diverterless Supersonic Inlet (DSI), is utilized with a three-dimensional bump to provide both supersonic flow compression and boundary layer diversion. Experiments were conducted at the presence of a typical fore-body including an elliptical nose to further contemplate the effects of fore-body geometry on the approaching flow. All tests were conducted at a constant free stream Mach number, $M_\infty = 1.65$ zero degrees angle of sideslip (*AOS*), and at various angles of attack (*AOA*) ranging from -2 to 6 degrees. The results showed that the present DSI had acceptable performance characteristics for all ranges of *AOA* tested. It should be noted that the present DSI does not have any moving, adjustable or auxiliary mechanisms as such systems or mechanism are used to improve the performance of an inlet.

Keywords: Supersonic flow, Diverterless inlet, Bump, Angle of attack, Boundary layer control

NOMENCLATURE

AIP	Aerodynamic Interface Plane
AOA	Angle of Attack
AOS	Angle of Sideslip
D	diameter
DC	distortion coefficient
DSI	Diverterless Supersonic Inlet
ECL	External centerline
ICL	Internal centerline
IBAR	Inlet Blocked Area Ratio
IEAR	Inlet Exit Area Ratio
L	length
LN	Left Nose
LB	Left Bump
LC	Left Cowl lip
LM	Left Main duct
MFR	Mass Flow Rate
M	Mach number
P	pressure
r	radius
Re	Reynolds number
RCS	Radar Cross Section
SOL	Shock on Lip
SBLI	Shock-Boundary Layer Interaction
TPR	Total Pressure Recovery
X	axial position
x	*x*-coordinate
y	*y*-coordinate
z	*z*-coordinate

Subscripts

i	in
o	out
s	static
p	plug
t	total
ϕ	rake angle
∞	infinity or free stream

1. INTRODUCTION

A supersonic fighter equipped with jet engine should be capable of flying effectively for a wide range of its flight envelope i.e.: Mach number, altitudes, angle of attack, etc. A supersonic inlet as the first component of the propulsion system, should be designed to provide the required air flow with an acceptable level of energy (high-pressure recovery) and quality (low distortion) and of course, it has to

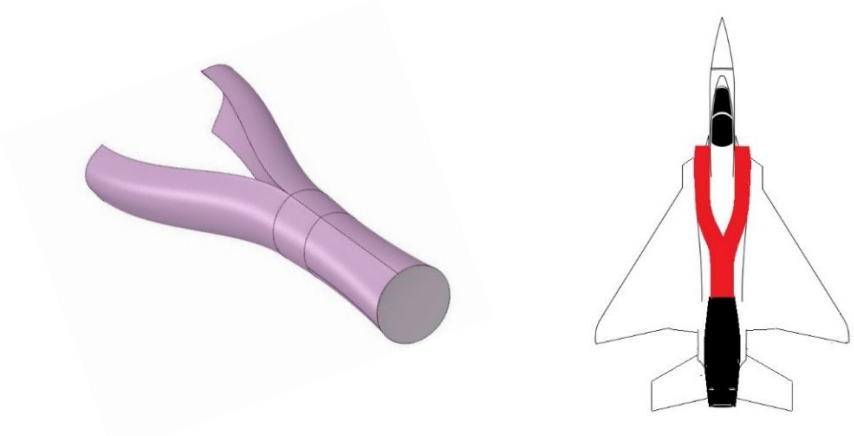

a) A *Y-shaped* inltake geometry

b) Location of *Y-shaped* intake in a typical fighter

Fig. A Y-shaped geometry and its installation location in a typical fighter aircraft

have minimum drag too (Mattingly and Von Ohain 2006; Soltani and Sepahi-Younsi 2015). Single engine supersonic fighter's propulsion system generally consists of twin intake ducts which are known as *Y-shaped* intakes. This type of intake is used in various fighters. Isometric view of a *Y-shaped* intake is shown in Fig. 1(a). In addition, its location is illustrated in a schematic view of a fighter aircraft in Fig. 1(b).

Supersonic inlets are designed and integrated with aircraft in various configurations and classifications such as supersonic flow compression region, flow dimensions and installation position, etc. (Seddon and Goldsmith 1999; Soltani, Daliri, and Younsi 2016). Depending on the maximum flight velocity of the aircraft, a special level of supersonic flow compression would be implemented. Furthermore, the designs and construction of supersonic inlets become highly complicated as the vehicle's Mach number is increased. For high speed flows, $\boldsymbol{M}_{\infty}\geq 2$, the required compression is achieved through multi-stage manner (double and multiple ramps or cones) which has been proved to have a better performance criterion in comparison with a single-stage one (Askari and Soltani 2018; Seddon and Goldsmith 1999).

The combination of oblique or normal shock waves formed on the compression surface, known as the shock system, provides external supersonic flow compression. The inlets are designed in such a way that when operating in the proximity of their design point, the corresponding shock waves impinge at a point on the cowl lip, called impingement point. This condition is known as the Shock on Lip (SOL) and provides maximum inlet mass flow with a minimum spillage drag and is used to calculate the critical operating condition of an external compression supersonic inlet. However, as stated, an aircraft encounters various flight conditions where the impingement point might be located away from the cowl lip. In such situations, variable structures are usually utilized to adjust the inlet geometry in order to recover the aforementioned SOL condition.

Depending upon the type of inlet, in practice, different forms of variable geometries are implemented to minimize the spillage flow. For a 2D or a ramped external-compression inlet, a hinged wedge is used to control the angles of the compression system and is usually considered to be the most appropriate form (Seddon and Goldsmith 1999). However, the variable geometry, its design, and construction requirements have significant complexity. In addition to the design, manufacturing, and maintenance costs, these systems have other disadvantages too.

In the past decades, the bumped inlet or Diverterless Supersonic Inlets (DSI) have attracted designer's attention and are now used in the new generations of fighter aircraft because of its fixed geometry, low weight and no additional system or variable structure. It should be noted that for a fighter aircraft, where engines are located inside the fuselage, the inlets are inevitably integrated with the body due to aerodynamic and weight requirements to name a few. For such inlets, the incoming boundary layer, formed on the aircraft fore-body, will deteriorate the inlet performance significantly. Therefore, to prevent this situation, various methods and devices such as a diverter, splitter plate, passive or active bleed control mechanism, etc. (or a combination of these methods) have been developed and implemented alongside these types of inlets. Fig. 2 shows a few of these design varieties. Diverterless Supersonic Inlets, DSI, utilize a fixed bump geometry to produce supersonic flow compression and further to prevent the incoming boundary layer to enter the inlet or at least reduce its thickness significantly (Hamstra *et al.*, 1998; Hamstra and Sylvester, 1998; Seddon and Goldsmith, 1999).

Simon *et al.* (1957) conducted wind tunnel experiments on a body integrated external ramped or bumped type inlets incorporating various types of the boundary layer bleed and the bypass duct. They studied an external bumped inlet in a direct comparison with a traditional two-dimensional compression ramp and reported a better satisfactory

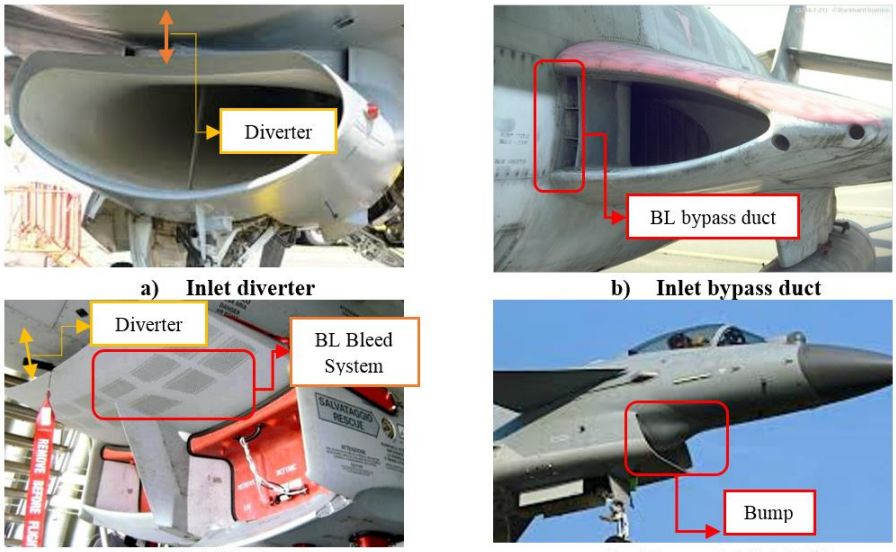

a) Inlet diverter **b) Inlet bypass duct**

c) Inlet bleed system **d) Bumped inlet (DSI)**

Fig. 2 Different methods implemented for boundary layer removing from inlet entrance.

operational stability over the range of Mach numbers tested, M_∞ =1.5–2.05, for the bumped type inlet. Although they used bumped inlet configuration to compress supersonic airflow, they applied a bypass duct in combination with the bump to remove the boundary layer (Simon, Brown, and Huff 1957). The bump concept is discussed by J. Seddon and E. L. Goldsmith (Seddon and Goldsmith 1999) as "a raised compression surface". The concept of the DSI system was first presented by Hmastra *et al.* in 1998 (Hamstra and Sylvester, 1998). They introduced and patented a DSI system including a "bump" that was utilized with an isentropic compression surface. They claimed that this system, which did not accommodate any moving part would reduce the complexity of the inlet system; such as boundary layer diverter, splitter plate, boundary layer bleed system or an overboard bypass system. (Hamstra *et al.*, 1998; Hamstra and Sylvester 1998). Tillotson *et al.* (2009), experimentally investigated supersonic flow field surrounding a bump compression surface geometry (without cowl lip) and compared their results with a wedge one at a free stream Mach number of M_∞=3. Their detailed study included the flow field surrounding the bump exclusively (Tillotson *et al.*, 2009).

Kim *et al.* (2007) numerically studied a three dimensional bumped type inlet which was a modification of a conventional ramped type one previously used by Loth *et al.* (2004). Please note that the present authors simulated this inlet three-dimensionally and investigated its shock boundary layer interaction (Askari and Soltani, 2018). Kim *et al*. further, studied the performance of supersonic inlets incorporating various three-dimensional bumps numerically (Kim and Song, 2008). Their simulations included effects of the geometrical features of the bump to control the interaction of shock wave and boundary layer at a free stream Mach number of M_∞=2 (Kim, Song, and Lim, 2007; Kim and Song, 2008; Kim, 2009).

Masud *et al.* (2011), numerically investigated performance of a DSI integrated with an aircraft typed body at low angles of attack, for both subsonic and supersonic Mach numbers of 0.8 and 1.65 respectively. In addition, they investigated flow field and performance characteristics for the same model but equipped with a passive bleed system in the vicinity of the designed mass flow rate of the intake at the same conditions. However, to the authors' knowledge, they have not reported any data or their simulation results about the effects of angle of attack on the inlet performance yet (Masud and Akram, 2011).

As it is concluded from the above short review of the literature, almost all of the previously published information has mainly focused on the advantages of the bumped inlets as a compression surface and (or) boundary layer remover devices. Although all of those researches are extremely useful in understanding the advantages or disadvantages of the bumped inlets, however, there has not been a comprehensive understanding about the supersonic flow over a DSI and the subsequent subsonic flow through its diffuser. Furthermore, the effects of other parameters such as nose shape, nose length, various diffuser design parameters, the number of inlets, angles of attack, etc. on the flow field of body integrated inlets have not been investigated yet. It is, therefore, useful to extend our understanding of DSI that includes at least a few of the aforementioned parameters. For this purpose, a comprehensive wind tunnel tests on a twin intake, body integrated DSI model has been carried out and a part of the results will be presented in this paper. In this regards the present authors, experimentally investigated the performance of a body integrated DSI at its critical, subcritical and supercritical operating conditions at a free stream Mach number of $M_\infty = 1.65$ (Soltani and Askari 2019). The results showed that the bump geometry used in the current design of DSI has an acceptable performance in the supersonic flow

compression as well as the boundary layer diversion. In addition, the existing DSI has a relatively wide range of stability in its subcritical operating conditions and has acceptable performance characteristics during its operation in both subcritical and supercritical cases.

It is, therefore, the intent of the ongoing study to investigate the performance of a body integrated Diverterless Supersonic Inlet at different angles of attacks and at a constant free stream Mach number of $M_\infty = 1.65$. There are several studies on the effects of *AOA* on various types of both subsonic and supersonic inlets. Krone and Friedrichs (2014) studied the inlet distortion sources and reported that during the maneuvering conditions significant transitory instabilities could occur if the angles of attack deviate from that of the aircraft's design condition (Krone and Friedrichs 2014). Kevin *et al.* (1997), reported a fundamental investigation of the effects of high angles of attack on the aerodynamic characteristics of an F/A-18A aircraft. They reported that as the *AOA* was increased, the trend of loss in the inlet recovery was similar to the trend of higher levels of turbulence (Walsh *et al.*, 1997). Saha *et al.* (2007), numerically investigated the effects of *AOA* on a twin inlet duct (*Y-shaped* intake). Their results showed an increase in the flow non-uniformity based on the total pressure distortion at the exit plane as the angle of attack was varied. In addition, they reported a shift in the high-velocity core vortices towards the bottom wall as the angle of attack was increased. (Saha, Singh, and Seshadri 2007)

Namkoung *et al.* (2012) numerically investigated the effects of *AOA* on a supersonic axisymmetric intake. They reported that by increasing the *AOA* from 3º to 10º, distortion increased up to 30% which is believed to be due to the axisymmetric (or three-dimensional) shock structures affected by the *AOA* variation (Namkoung *et al.*, 2012). Trefiny *et al.* (2014) experimentally investigated the effects of angle of attack on a supersonic ramped inlet equipped with an elliptical cowl and reported an abrupt decrease in both total pressure recovery and mass flow ratio (Trefny *et al.*, 2014). Soltani and Farahani (2012) investigated the effects of angle of attack on the performance and stability margin of an axisymmetric supersonic intake (Soltani and Farahani 2012). As noted, there is limited data on the effects of angle of attack on the DSI inlets, therefore, in the present investigation, the effects of angle of attack on the performance of a Diverterless Supersonic Inlet are investigated. The model is equipped with a Y-shaped intake which includes two inlets integrated with the body at its both sides. The flow after passing through these inlets is mixed before reaching the engine face. The inlet performance is investigated at a free stream Mach number of $M_\infty = 1.65$ and at various angles of attack ranging from -2 to 6 degrees. The angle of sideslip is set to zero degrees for all test presented in this paper. To investigate the inlet performance characteristics, the static pressure distribution along the centerline of inlets and model fore-body, which undoubtedly affects the inlet performance especially for non-zero *AOA*, is measured with sensitive pressure transducers. Moreover, several pressure transducers are placed at the engine face, known as Aerodynamic Interface Plane (AIP), to measure the total pressure at this section for calculation of the inlet performance parameters. A brief description of the experimental setup, wind tunnel tests implementation and results are presented in the following sections. For a detailed description of the facility pleases see Soltani and Askari (2019).

1. EXPERIMENTAL SETUP

1.1. Wind Tunnel

The supersonic wind tunnel used in these experiments is an open circuit suction type, with a rectangular 60×60 cm^2 test section. This tunnel can operate continuously for ranges of Mach numbers, M_∞=0.4–2.5, with no limitation on the running time (Soltani, Farahani, and Kaji 2011). The tunnel was calibrated for different free stream Mach numbers. Various flow parameters, such as flow uniformity, flow angularity, and turbulence intensity were measured and found to be within the acceptable range for this type of wind tunnel (Soltani and Farahani 2013). The turbulence intensity in the test section was reported to vary from 0.4% to 1.4% (Soltani and Farahani 2012). The free stream Mach number is attained by a variable nozzle through a jet engine located on both sides of the second diffuser. At the DSI designed Mach number, M_∞ =1.65, maximum flow angularity in the test section was measured and found to be about 0.5 deg.

There are porous bleed holes on the upper and lower walls of the test section that can stabilize and control wind tunnel shock and other reflected waves as well as controlling the boundary layer thickness. Side-wall windows of the test section make it possible to observe the flow and shock pattern by means of Schlieren or Shadowgraph visualization systems (Soltani, Younsi, and Farahani 2015; Soltani and Sepahi-Younsi 2015). The current wind tunnel tests were conducted for various *AOA* at a free stream Mach number of M_∞=1.65. A schematic view of the *AOA* mechanism is shown in Fig. 3. All tests are conducted at zero degrees angle of sideslip.

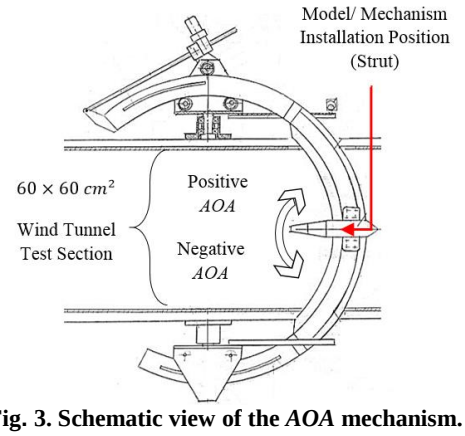

Fig. 3. Schematic view of the *AOA* mechanism.

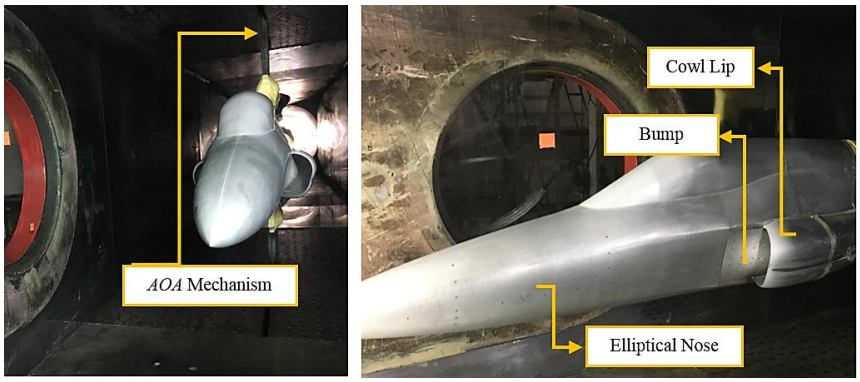

Fig. 4. Three views of the model installed in the test section.

1.2. Model

Figure 4 shows three views of the twin inlet wind tunnel model used in the present experiments which are installed on the C-type *AOA* mechanism inside the test section. It is a three-dimensional supersonic external compression inlet known as "Bumped Inlet" or "Diverterless Supersonic Inlet". All tests were performed in the presence of a typical aircraft fore-body comprising of an elliptical nose to closely simulate the effects of upstream flow and the corresponding boundary layer growth. A fixed three-dimensional bump geometry is used for both boundary layer diversion and external supersonic flow compression. The model was installed at the center of the wind tunnel test section in such a way that it could be rotated along the *x*-axis for possible flow visualization in the regions of inlet compression surface where the shock system forms during supersonic tests.

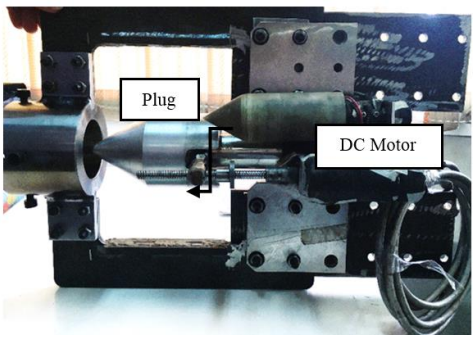

Fig. 5. Mass flow rate control mechanism.

The total blockage ratio (which is defined as the ratio of the projected model cross section area to the wind tunnel test section) at both zero degrees angles of attack and zero degrees sideslip angle was 3%. For the maximum value of *AOA*, 6°, the blockage ratio was 0.5%. The inlet mass flow rate was controlled via movement of a conical plug located at the end of the model and was able to move along the inlet center-body by a small DC-motor and a ball screw, Fig. 5. All results presented in the current study are for the design mass flow condition, known as the critical condition, detailed of which is given in Soltani and Askari (2019).

1.3. Pressure Sensors and Their Locations

The data for all pressure ports were collected simultaneously. To calculate the inlet performance parameters (*MFR*, *TPR* and AIP distortion) steady measurements were considered and data for all sensors were acquired for 5 seconds. Two types of pressure transducers, low and high frequency, were used in the present experiments. Both sensors were of differential-type pressure transducers (Sepahi-Younsi and Soltani 2015). Total of fifty-six pressure transducers was used for measuring the static pressure along the model and inlet (44 sensors) and total pressure at the AIP rake (12 sensors) as shown in Fig. 6. The sensors were numbered based on their locations on each component of the model. The letters "LN", "LB" "LC", "LM", and "TR" denote Left Nose, Left Bump, Left Cowl, Left Main and Total Rake pressure, respectively. Red and black numbers represent high and low-frequency pressure transducers, respectively, Fig. 6. The details of sensor types, positions, and uncertainties of the pressure transducers are presented in Soltani and Askari (2019). An isometric view of the locations of sensors on the wind tunnel model is illustrated in Fig. 7.

For the Total rake (or AIP rake), denoted by "TR", twelve pressure transducers were used to measure the total pressure distribution and its variation with different conditions at the AIP. In addition, four pressure transducers were located at the AIP position (LRS, RRS, URS, and DRS) to measure the mean value of the static pressure at this station, see Fig. 6. Moreover, the total pressure measurements via the specially designed rake were used to calculate the inlet performance parameters, *MFR*, *TPR* as well as the AIP distortion.

The intake performance is investigated using non-dimensional static pressure (or pressure ratio) distribution along the inlet in the stream-wise direction. Two colored lines are considered as the baselines for this investigation, a red line that passes from the left nose and the bump surface, called internal centerline (ICL), and an orange line which passes from the left cowl, called external centerline (ECL) in this paper, Fig. 6.

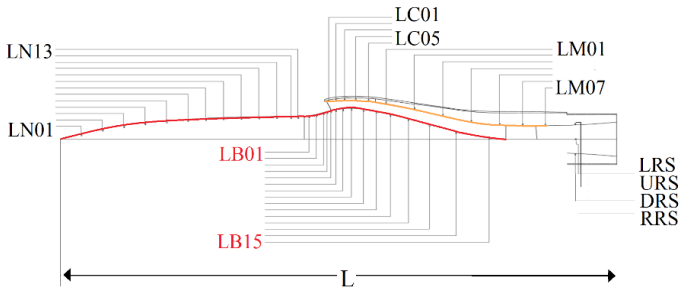

Fig. 6. Sensor numbers and locations on the wind tunnel model.

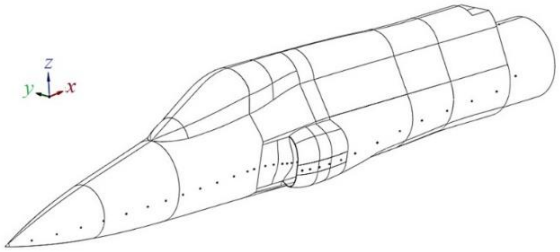

Fig. 7. Isometric view of sensor locations on the wind tunnel model.

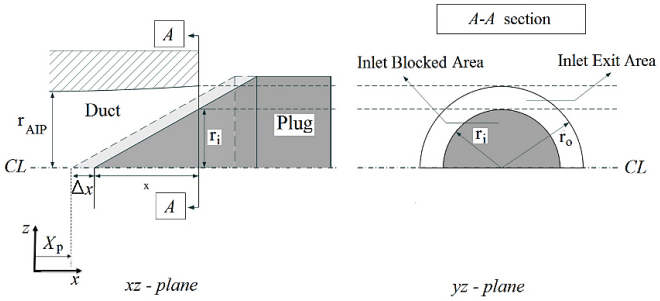

Fig. 8. Schematic plans of intake exit area and plug.

In addition, distribution of the non-dimensional total pressure (total pressure ratio) at the inlet AIP station is used to analyze the most important performance parameters. The total AIP multi-probe rake accommodates twelve total pressure probes and was located at the model AIP, $x/L = 0.93$. The rake could be rotated along the *x*-axis at two different angles of zero and 90 degrees to acquire total pressure at this station in both *y* and *z* locations. The AIP total pressure distribution for the design conditions of M_∞=1.65, *AOA*=0, and *IBAR*=0.35 is presented in Soltani and Askari (2019) along with a detailed explanation. The total pressure data are used to calculate the inlet performance parameters such as *TPR*, *MFR*, etc.

1.4. Flow Visualization System

A Schlieren flow visualization system was used in all tests to visualize the external shock system that forms in front of the inlet and the images were recorded at the same frequency that the data of the pressure transducers were collected. A detailed description of this system is presented in Soltani and Askari (2019). However, when the model is set to an *AOA* greater than zero, the present visualization set-up is not able to show images of the shock system.

1.5. Test Procedure

The effects of *AOA* on DSI performance are the main purpose of the current study. Therefore, all tests presented here are performed at the design mass flow rate condition and at a constant free stream Mach number of $M_\infty = 1.65$. For this purpose, five different *AOA* (-2, 0, 2, 4, and 6 degrees) are considered for these tests. Positive and negative directions of *AOA* variations are illustrated in Fig. 3. The Inlet Blocked Area Ratio (*IBAR*) defined as the ratio of the exit duct area blocked by the plug to the total exit area of the duct, is defined in the following equation, Eq. (1). When *IBAR* is 100%, it means that the exit area of the intake is completely closed and when it is 0%, it means that the exit area is completely opened. In addition, another parameter is defined as the Inlet Exit Area Ratio (*IEAR*) which determines the value of mass flow passed through the inlet for each plug condition, Eq. (2). Figure 8 illustrates the schematic plan of these definitions. This parameter has a behavior similar to the mass flow ratio parameter. By definition, for the critical condition: $IBAR = 0.35$ and $IEAR = 0.65$.

$$IBAR = A_{Plug} / A_{exit} \quad (1)$$

$$IEAR = 1 - IBAR \quad (2)$$

2. RESULTS AND DISCUSSIONS

2.1. Effects of Angle of Attack on the Static Pressure Distribution

The distribution of the static pressure ratio, $P_s/P_{t\infty}$, on the internal centerline, ICL, and on the external centerline, ECL, of the model at zero degrees *AOA* are presented in Fig. 9. Both static and total pressure values of the wind tunnel test section non-dimensionalized by the free stream total pressure, $P_{t\infty}$, are also plotted in the same figure. A Schlieren image of the shock wave formation is shown in Fig. 10 where it clearly illustrates the shock system as well as the boundary layer thickness in the proximity of the inlet compression surface. As is expected similar shock systems are formed on both inlet supersonic compression surfaces, Fig. 10. The flow pressure ratio decreases passing over the nose component, LN01-LN13, then increases passing thru the shock system, LN13-LB06. A slight decrease in flow pressure ratio is seen at the throat location and it increases again till exit the inlet diffuser, see Fig. 9. Detailed description of the variation of $P_s/P_{t\infty}$ along both ICL, ECL, and the Schlieren images for this condition, $M_\infty = 1.65$, *AOA*=0°, and *IBAR*=0.35, is given in Soltani and Askari (2019). Figure 11 shows the measured static pressure ratio distribution along both ICL and ECL for various angles of attack. However, since the effects of angle of attack on the pressure distribution along various parts of the model cannot be clearly seen from Fig. 11, pressure ratio values for several locations along ICL that includes the nose, body, bump, and ECL, which includes the cowl and the main diffuser, is shown in Fig. 12a-l. Form Fig. 12(a), it is seen that the pressure sensed by the first transducer located at x/L=3.8%, increases as the *AOA* is increased. This variation is due to the changes in the shock wave strength formed at the nose and cross flow components over the nose and the body. As the angle of attack is increased (positive *AOA*), shock wave strength over the lower portion of the body increases while its strength over the upper surface decreases until at a certain angle of attack, an expansion wave forms over the leeward section of the body. For the negative angles of attack, the situation is reversed, i.e., the shock strength on the lower surface decreases while that of the upper surface, windward portion, increases. In addition, for the positive angles of attack, the cross-flow component of the velocity behind the shock wave moves from the lower surface of the body to the upper surface and vice-versa for the negative angles of attacks. At the end of the nose, x/L=19%, Fig. 12(b), the static pressure does not vary significantly with angles of attack as it is expected. At x/L =37%, farther from the nose, the pressure ratio variation with the angle of attack is seen to be similar to that at x/L =3.8%, however, the magnitudes differ significantly, Fig. 12(c).

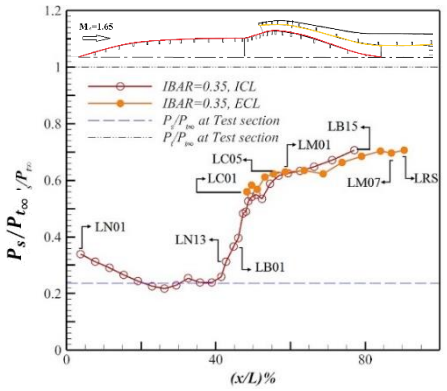

Fig. 9. Static pressure ratio distribution along the ICL and ECL at the critical condition, *AOA*=0°.

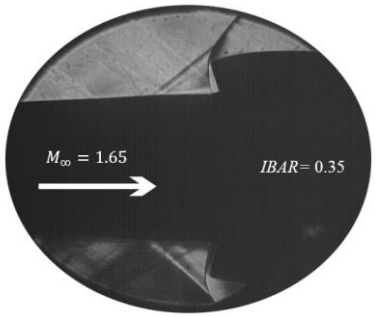

Fig. 10. Schlieren image of inlet model at its critical operating condition, *AOA*=0°.

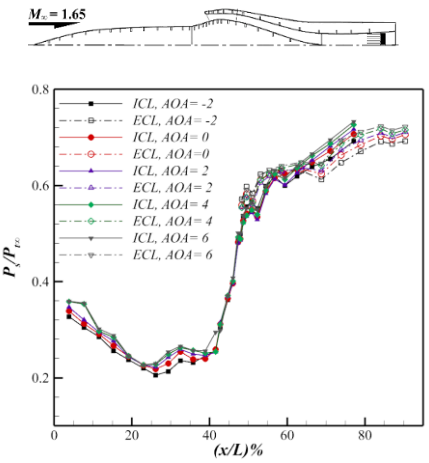

Fig. 11. Static pressure ratio distribution on the ICL and ECL for various degrees of *AOA* at M_∞=1.65.

From x/L =45% till x/L =49%, Fig 12d-f show pressure variation with angles of attack in the vicinity of the bump, and approximately midway over the bump surface respectively. From these figures, it is clearly seen that varying angles of attack do not influence the pressure ratio significantly. In other words, there are no significant variations in the pressure distribution on the compression surface as the *AOA* increases or decreases, in comparison with the pressure variations seen on other components. Figure 13(f) clearly shows that the pressure distributions on the bump centerline behave almost

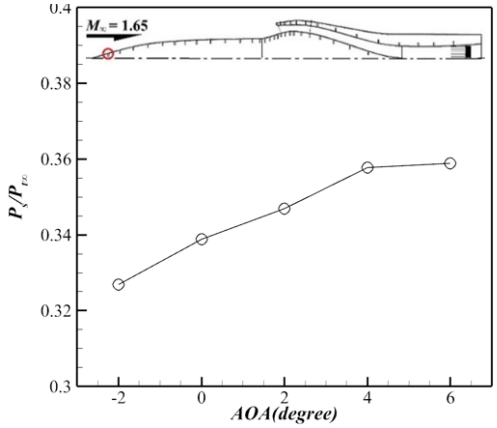

a) LN01, $x/L = 3.8\%$ (Near the nose)

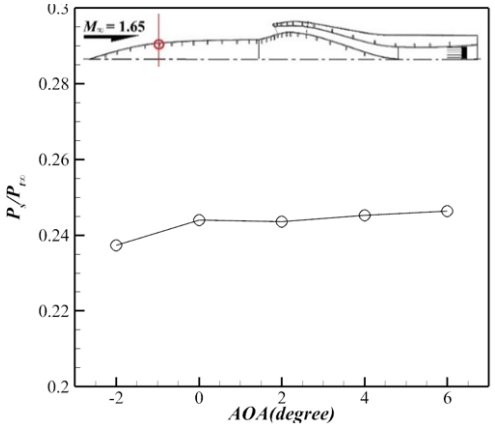

b) LN05, $x/L = 19\%$ (End of the nose)

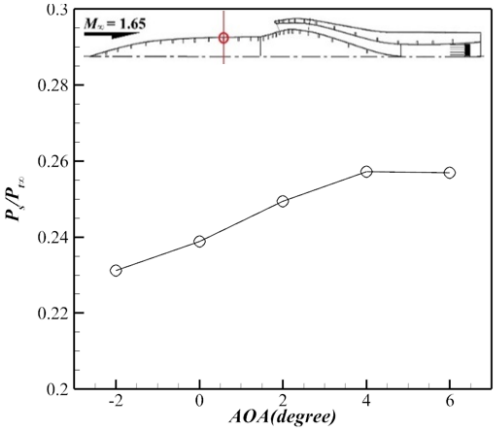

c) LN10, $x/L = 37\%$ (Over the body)

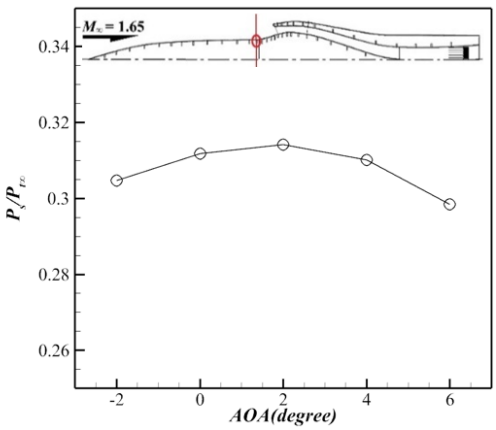

d) LN13, $x/L = 43\%$ (Close the bump)

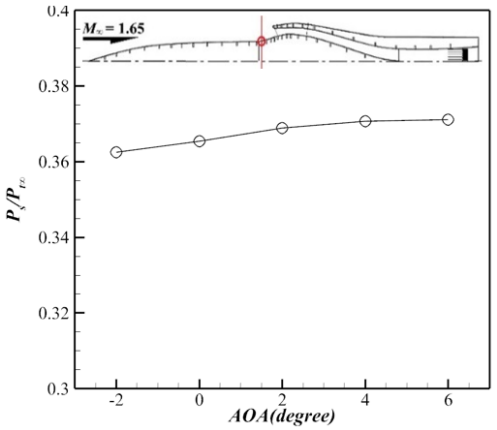

e) LNB01, $x/L = 45\%$ (Beginning of the bump)

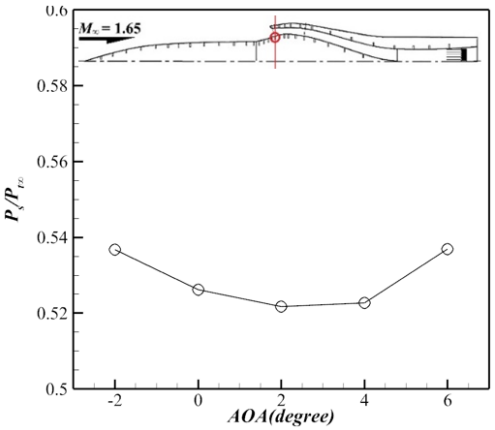

f) LB05, $x/L = 49\%$ (Inlet entrance)

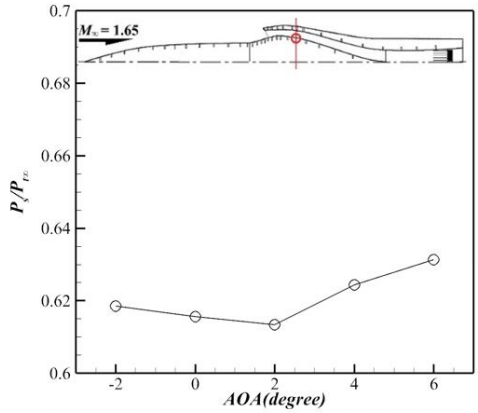

g) LB10, $x/L = 57\%$ (Left hand side limb of the inlet diffuser)

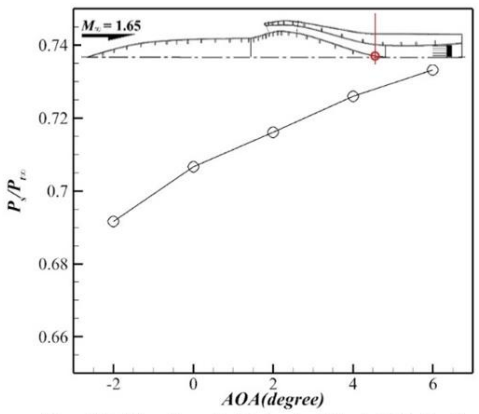

h) LB15, $x/L = 77\%$ (end of the left limb, flov attachment location)

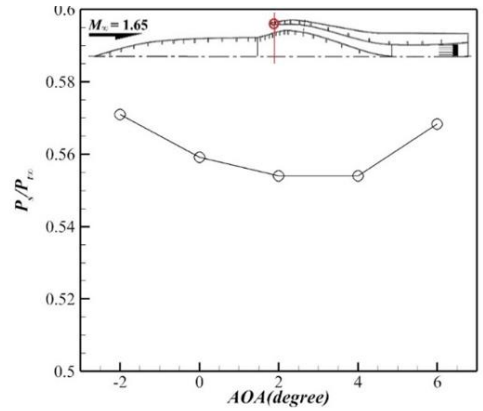

i) LC01, $x/L = 48\%$ (Cowl lip)

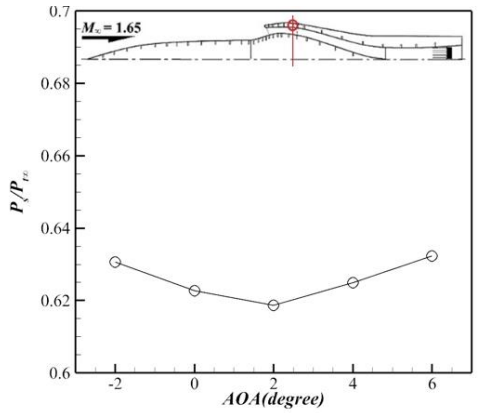

j) LC05, $x/L = 56\%$ (Cowl)

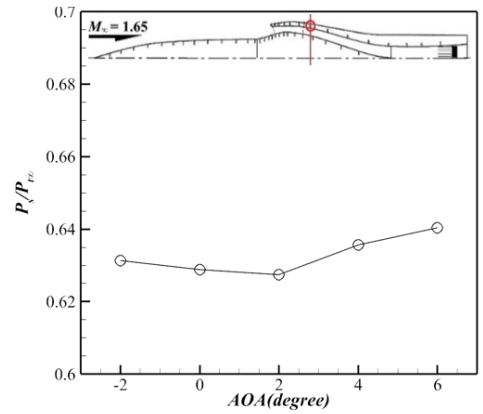

k) LM01, $x/L = 59\%$ (Main duct)

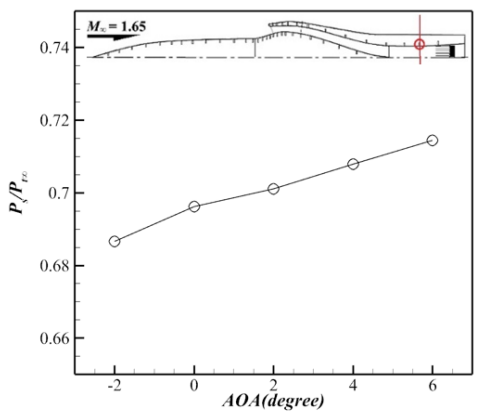

l) LM07, $x/L = 87\%$ (Main duct)

Fig. 12. Effect of *AOA* on the various components of the model, a-l, *IBAR*=0.35, $M_\infty = 1.65$.

symmetrically with respect to increasing or decreasing the *AOA*. However, it is seen that the variations for the negative angles of attack are higher than those of the positive angles, Fig. 12(f). The authors believe that this is due to the installation of the bump in the ventral positions related to the body in the present inlet-body integrated configuration. In such a situation, the bump surface, especially in its lower half, experiences free stream supersonic flow which has encountered the body curvature and accelerates toward the bump compression surface. As a result, from observing the static pressure distribution at the bump centerline, it seems that the bump configuration does not significantly disturb the flow field at least at the centerline during *AOA* variations as it occurred for other parts of the body, x/L =3.8% and x/L =37%. In other words, the

bump geometry shifts the value of pressure at x/L =45% to a specific value almost equal to the bump compression ratio and delivers it to the inlet diffuser, x/L =49%. Figure 12(g) shows pressure variations with angles of attack for a sensor located at x/L =0.57, diffuser part of the inlet, as seen from Fig. 6. This figure shows that as the angle of attack increases from zero to two degrees, a slight reduction in the pressure ratio is attained, however by further increasing the angle of attack, pressure ratio increases. Furthermore, the pressure variations shown for this part of the inlet are seen to be relatively invariant with angles of attack.

Finally, for the sensor located at x/L =77%, Fig 12(h) end of the inlet diffuser limb, the pressure ratio increases as the angles of attack is increased. Static variations of the pressure ratio along the cowl, Fig. 12i-j, and along the left main duct, Fig 12k-l, are similar to the variations seen for the bump and diffuser limb, Fig. 12f-h. Overall, it is apparent that the main source of pressure variations along different components of the model, body, inlet, AIP, etc., is the variations of the oblique shock strength formed at the nose tip.

Figure 13a-b shows the relative comparisons of the variations of pressure along both ICL, Fig 13(a), and ECL, Fig. 13(b), with angles of attack to the clean component and are shown for $x/L > 40\%$. The relative variation in percentage is defined as:

$$Delta\left(\frac{P_s}{P_{t_\infty}}\right)\% = \left(\left(\frac{P_s}{P_{t_\infty}}\right)_{at\ AOA} - \left(\frac{P_s}{P_{t_\infty}}\right)_{at\ zero\ AOA}\right)\%$$

Figure 13(a) indicates that up to $x/L = 0.48\%$, delta pressure ratio variations along ICL is not well defined, however, beyond this point this figure shows that as the angle of attack is increased delta pressure ratio variation is well defined. Minimum delta pressure ratio for all angles of attack occur around $x/L = 0.59\%$ which is located inside the inlet, beyond the throat. The delta static pressure beyond this point, $x/L = 0.59\%$, varies significantly with angles of attack and seems to reach a steady value around $x/L = 0.78\%$. A similar trend is observed in Fig. 13(b), which shows delta pressure ratio variations along ECL with angles of attack. However, this figure shows that the maximum value of the delta pressure ratio along ECL occurs around $x/L = 0.75\%$ for all angles of attack. Beyond, $x/L = 0.75\%$, it is seen that delta pressure ratio for all angles of attack decreases toward zero values, Fig. 13(b).

2.2. Effects of *AOA* on the Performance of DSI

To investigate the effect of *AOA* on the performance of the present DSI, the relative parameters such as mass flow rate, total pressure recovery and AIP flow distortion were calculated. All of these variables need integration of the total pressure at the inlet AIP. Therefore; the total pressure distribution at the inlet AIP are plotted for the different angles of attacks using both horizontal and vertical total pressure distributions measured at this station via the AIP multi-probes rake. The data are presented in Fig. 14a-e. The circle on the top of Fig. 14, is shown to clarify the AIP right, left, up and down stations mentioned in this figure. The low energy flow distribution is shown with blue regions (corresponding to lower values of P_t/P_{t_∞}) while the higher energy flow is shown with yellow color (corresponding to higher values of P_t/P_{t_∞}). As it is evident, the distributions are relatively seen to be symmetric for the left and right sections of the AIP flow distributions at zero degrees angle of attack, Fig. 14-b.

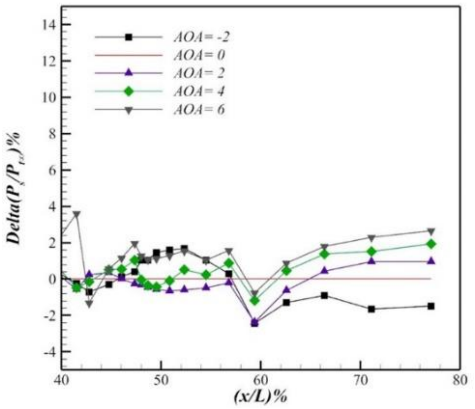

a) ICL

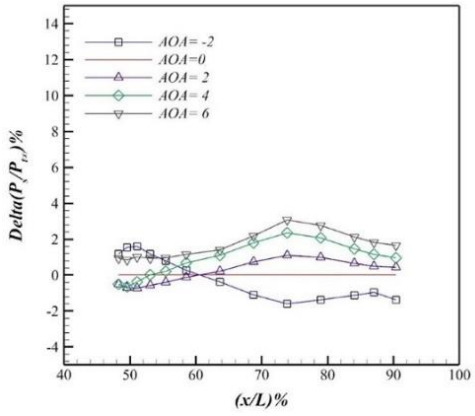

b) ECL

Fig. 13. Relative comparison of pressure variation along the model, *IBAR*=0.35.

There exist higher total pressure distributions near the lower portion of the AIP in comparison with its upper portion for *AOA*= -2 to 2 degrees, Fig. 14a & c. In other words, the internal core flow is located in the lower half of AIP. For *AOA*=6 degree, however, it is clearly seen that the internal core flow has shifted toward the upper half, AIP up, of the inlet, Fig. 14(e).

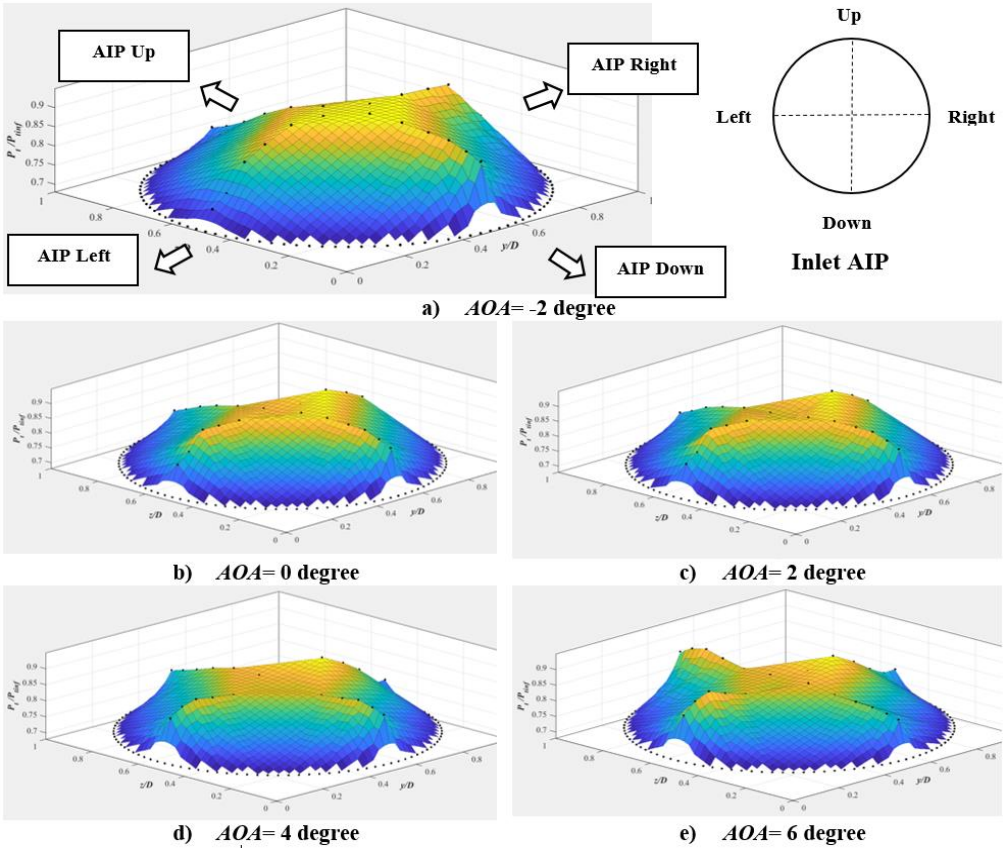

Fig. 14. Total pressure distribution at the engine face (AIP)

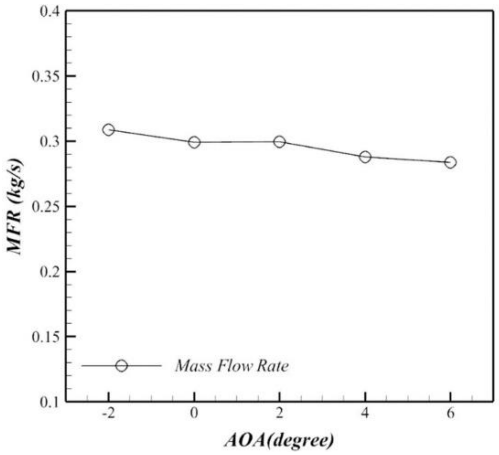

Fig. 15. The DSI mass flow rate versus *AOA* variation, *IBAR*=0.35.

Figure 15 shows the mass flow ratio variations as the *AOA* is increased from -2 to 6 degrees. It is seen that the mass flow rate slightly decreases when the *AOA* is increased. However, it seems that these variations are not significant for the ranges of *AOA* tested in this study. At the worst condition, *AOA*=6º, the mass flow rate varies about 5% with respect to its value for the zero-degrees angle of attack case. Figure 16 shows the total pressure recovery (*TPR*) variations for the present DSI as the *AOA* is varied. Again, it is apparent that *TPR* remains relatively constant for angles of attacks examined here. At an *AOA*=6º, *TPR* is seen to improve about 0.8% in comparison with that of the zero-degrees angle of attack case. The variations of distortion coefficient, *DC*, versus *AOA* are shown in Fig. 17. The *DC* at the engine face position of the present DSI remains below 0.08 for all angles of attacks. It seems that the symmetrical shape of the bump compression surface used in this DSI configuration causes the inlet flow quality demonstrated by the total pressure recovery and distortion coefficient to remain relatively invariant with angles of attack as verified by the measured experimental data.

Figure 18 shows the DSI performance curve at the zero-degrees angle of attack, Soltani and Askari (2019), as well as its variation at different angles of attack for the same *IBAR*, *IBAR*=0.35. It is clearly seen that as the *AOA* increases or decreases, the DSI performance point varies slightly from the designed performance curve shown by the dash-dotted line in Fig. 18. This indicates that for these ranges of angles of attack, the present intake will not encounter flow instability or significant flow distortions. From the measured data, it is deduced that for the positive *AOA* the DSI performance point in the *MFR*-*TPR* graph moves toward the inlet subcritical conditions, while for the negative *AOA* it shifts toward the supercritical case.

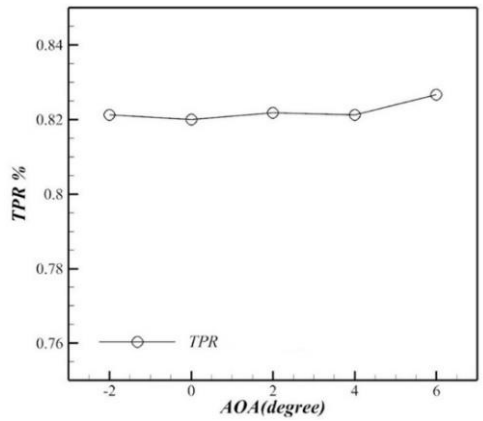

Fig. 16. The DSI pressure recovery versus *AOA* variation, *IBAR*=0.35.

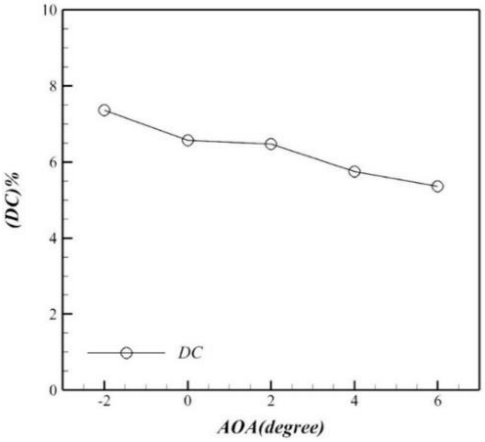

Fig. 17. The DSI distortion versus *AOA* variation, *IBAR*=0.35.

It is therefore concluded that the present DSI has acceptable performance characteristics for these ranges of angles of attack. These levels of flow stability and inlet performance are highly desirable for a supersonic inlet as it may encounter angles of attack variations during the flight. It should be noted that the present DSI has no moving, adjustable, variable structure and no auxiliary mechanism or system. However, these mechanisms could be used to further improve its performance.

3. CONCLUSION

Experimental studies about the effects of angle of attack variations on the performance of a body-integrated supersonic inlet have been carried out. The present inlet, known as Diverterless Supersonic Inlet (DSI), is utilized with a three-dimensional bump to provide both supersonic flow compression and boundary layer diversion. In order to model the effects of the fore-body geometry on the inlet approaching flow, the present experiments were conducted at the presence of a typical fore-body including an elliptical nose. All experiments were performed at a constant free stream Mach number of $M_\infty = 1.65$, zero degrees angle of sideslip (*AOS*), and at various angles of attack ranging from -2 to 6 degrees. The results showed that the pressure distribution on the nose increases as the *AOA* is increased and vice-versa. The pressure distributions on the bump centerline showed relatively similar behavior for all angles of attack examined here. However, it is seen that for the negative angles of attack, the variations are more notable than those for the positive angles.

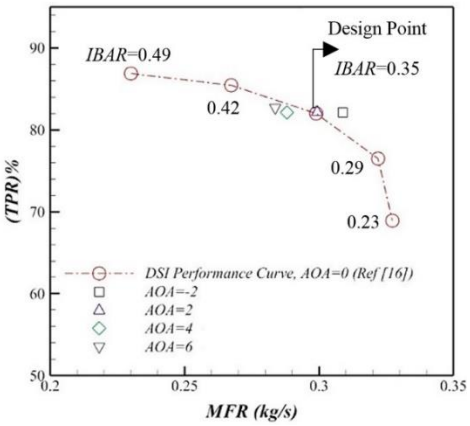

Fig. 18. The DSI performance curve at zero degree *AOA* and its variation at different degrees *AOA, IBAR=0.35*.

In the diffuser, the trend described for the bump compression surface continues to a location in the divergent portion of the bump. As a result, for a fixed inlet blocked area ratio, *IBAR*=0.35, the static pressure at the AIP increases as the *AOA* is increased. The static pressure distribution at the bump centerline shows that the bump configuration does not significantly disturb the flow field (at the centerline) during *AOA* variations in comparison with other types of compression surfaces such as cone or ramp. Variations of angles of attack seem to have significant effects on the total pressure distribution at the engine face, AIP. It shifts the core of internal flow from the lower half of the AIP for a negative angle of attack to its upper half for positive ones.

The present DSI mass flow rate slightly decreases when the *AOA* is increased. For the highest angle of attack tested, *AOA*=6º, the mass flow rate varied only about 5% in comparison with the zero-degrees angle of attack case. *TPR* remains also relatively fixed for these ranges of angles of attack. The *DC* at the engine face position of the present DSI remains below 0.08 and as the *AOA* is increased or decreased, the DSI performance point shifts away from the DSI designed performance curve. As a result, for the positive *AOA*, the DSI performance point in *MFR-TPR* graph budges toward the subcritical conditions and for the negative *AOA*, it deviates toward the supercritical one. From the present experimental data, it is concluded that the present DSI has an acceptable performance characteristic for the ranges of *AOA* tested. These levels of flow stability and inlet

performance quality are highly desirable for a supersonic inlet as it might encounter angles of attack variations during the flight.

REFERENCES

Askari, R. and M. R. Soltani (2018). Two-and three-dimensional numerical simulations of supersonic ramped inlet, *Scientia Iranica, Transactions B: Mechanical Engineering*, 25(4), 2198-2207.

Hamstra, J. W. and T. G. Sylvester (1998). System and Method for Diverting Boundary Layer Air, U.S. Patent No. 5, 779, 189.

Hamstra, J. W., B. N. McCallum, T. G. Sylvester, B. W. Denner and J. A. Moorehouse (1998). Transition Shoulder System and Method for Diverting Boundary Layer Air, U.S. Patent No. 5, 749, 542.

Kim, S. D. (2009). Aerodynamic Design of a Supersonic Inlet with a Parametric Bump. *Journal of Aircraft* 46(1), 198.

Kim, S. D. and D. J. Song (2008). Numerical Study on Performance of Supersonic Inlets with Various Three-Dimensional Bumps. *Journal of Mechanical Science and Technology* 22(8), 1640-1647.

Kim, S. D., D. J. Song and S. Lim (2007). A Numerical Analysis on Three-Dimensional Flow Field in a Supersonic Bump Inlet, *45th AIAA Aerospace Sciences Meeting and Exhibit*, AIAA 2007-0689, Nevada, 689.

Krone, J.-H. and J. Friedrichs (2014). Generation of Intake Distortion due to Angle of Attack for a High Bypass Turbofan Model, *ASME 2014 International Mechanical Engineering Congress and Exposition*.. American Society of Mechanical Engineers, November, V001T01A064-V001T01A064.

Loth, E., F. Roos, D. Davis, J. Mace, R. Jaiman, S. White, C. Dutton and C. Dutton (2004). Meso-Flap and Bleed Flow Control for A Mach 2 Inlet, *42nd AIAA Aerospace Sciences Meeting and Exhibit*, AIAA 2004-855, Reno, NV, 855.

Masud, J. (2011). Flow Field and Performance Analysis of an Integrated Diverterless Supersonic Inlet, *Aeronautical Journal* 115(1170), 471-480.

Masud, J. and F. Akram (2011). Effect of Passive Bleed System on an Integrated Diverterless Supersonic Inlet, *49th AIAA Aerospace Sciences Meeting including the New Horizons Forum and Aerospace Exposition*, AIAA 2011-920, Orlando, FL, 920.

Mattingly, J. D. and Von Ohain (2006). H., *Elements of Propulsion: Gas Turbines and Rockets*, 2nd ed., AIAA Education Series, AIAA, Reston, VA, 421-431.

NamKoung, H. J., W. R. Hong, J. M. Kim, J. S. Yi, and Ch. A. Kim (2012). Effects of Angles of Attack and Throttling Conditions on Supersonic Inlet Buzz. *International Journal of Aeronautical and Space Sciences* 13(3), 296-306.

Saha, K., S. Singh and V. Seshadri (2007). Effect of Angle of Attack on the Performance of Twin Intake Duct, *37th AIAA Fluid Dynamics Conference and Exhibit*, 4357.

Seddon, J., and E. L. Goldsmith (1999). *Intake Aerodynamics*, 2nd ed., AIAA Education Series, AIAA, Reston, VA, 268–292.

Sepahi-Younesi, J. (2015). *Experimental Investigation on Buzz Phenomenon Prediction in a Mixed Compression Supersonic Inlet.* PhD thesis, Dept. of Aerospace Engineering, Sharif Univ. of Technology, Tehran, Iran.

Simon, P. C., D. W. Brown and R. G. Haff (1957) *Performance of External Compression Bump Inlet at Mach Numbers of 1.5 and 2.0*, NACA Rept. RM-E56L19.

Soltani, M. R. and J. Sepahi-Younsi (2015). Buzz Cycle Description in an Axisymmetric Mixed-Compression Air Intake, *AIAA Journal* 54(3), 1040-1053.

Soltani, M. R. and M. Farahani (2012). Effects of Angle of Attack on Inlet Buzz. *Journal of Propulsion and Power* 28(4), 747-757.

Soltani, M. R. and M. Farahani (2013). Performance Study of an Inlet in Supersonic Flow, *Proceedings of the Institution of Mechanical Engineers, Part G: Journal of Aerospace Engineering* 227(1), 159-174.

Soltani, M. R. and R. Askari (2019). On the Performance of a Body Integrated Diverterless Supersonic Inlet, *Journal of Aerospace Science and Technology*.

Soltani, M. R., J. Sepahi-Younsi and A. Daliri (2016). Effects of Shock Wave/Boundary-Layer Interaction on Performance and Stability of a Mixed-Compression Inlet. *Scientia Iranica, Transactions B: Mechanical Engineering* 23(4), 1811-1825.

Soltani, M. R., J. Sepahi-Younsi and M. Farahani (2015). Effects of Boundary-Layer Bleed Parameters on Supersonic Intake Performance. *Journal of Propulsion and Power* 31(3), 826-836.

Soltani, M. R., M. Farahani and M. Asgari Kaji (2011).An Experimental Study of Buzz Instability in an Axisymmetric Supersonic Inlet. *Scientia Iranica* 18(2), 241-249.

Tillotson, B. J., E. Loth, J. C. Dutton, J. Mace and B. Haeffele (2009). Experimental Study of a Mach 3 Bump-Compression Flow Field. *Journal of Propulsion and Power* 25(3), 545-554.

Trefny, C.J., S.M. Hirt, B.H. Anderson, L. Fink and T. Magee (2014). Performance of a Supersonic Over-Wing Inlet with Application to a Low-

Sonic-Boom Aircraft *50th AIAA/ASME/SAE/ASEE Joint Propulsion Conference*, p. 3802.

Walsh, K. R., A. J. Yuhas, J. G. Williams and W. G. Steenken (1997). Inlet Distortion for an F/A-18A Aircraft During Steady Aerodynamic Conditions up to 60 Angle of Attack. *National Aeronautics and Space Administration*, Dryden Flight Research Center.